A New Quarter Concave Cylinder Linked Dihedral Reflector for Fully Polarimetric Calibration of Wideband Nonreciprocal Radar Systems

Xiaojian Xu, Tianjin Liu, and Pengfei Wu

***Abstract*— Traditionally, fully polarimetric calibration of a nonreciprocal radar system requires measurements of at least two passive calibrators, such as a dihedral corner reflector plus a metal plate or sphere. Interchanging measurements of multiple calibrators results in not only higher complexity but also degraded uncertainty. In this work, a new polarimetric passive calibrator is proposed, which is designed as quarter concave cylinder linked dihedral (QCCLD). The backscattering of a single QCCLD contains both depolarizing and nondepolarizing components when rotating along the radar line of sight (LOS). This unique characteristic makes it an excellent polarimetric calibrator, which allows fully polarimetric calibration of a nonreciprocal radar system by measuring just a single QCCLD. The theoretical polarimetric scattering matrix (PSM) is derived based on physical optics (PO). Using complex exponential (CE) model-based parametric representation, a novel polarimetric calibration procedure is developed to suppress undesirable scattering components, which degrade the calibration accuracy. Experimental calibration results are presented with the polarization isolation improvement of more than 15 dB over 6–18 GHz frequency band, demonstrating the usefulness of the proposed QCCLD calibrator for fully polarimetric calibration of a wideband nonreciprocal radar system.**

***Index Terms*— Electromagnetic (EM) scattering, nonreciprocal radar system, polarimetric calibration, polarimetric passive radar calibrator, polarimetric scattering matrix (PSM).**

I. Introduction

POLARIMETRIC scattering matrix (PSM) provides an exquisite description of the interaction between electromagnetic (EM) wave and radar target, which plays important roles in scattering diagnosis and target identification [1], [2]. In practice, antenna crosstalk and channel imbalance distort the received signal in polarimetric radar systems, which have to be solved through fully polarimetric calibration. There are mainly two tasks in polarimetric calibration of a radar system: 1) design an appropriate polarimetric calibrator, which has known theoretical PSM, and 2) develop measurement and processing procedures to obtain all the distortion parameters from measured data. Since the standard polarimetric calibration signal model has been proposed in the 1990s [3], [4], different polarimetric calibrators and improved calibration methods have been proposed for specific requirements [5], [6], [7], [8], [9]. Recently, in terms of the new calibrators, Monzon [10] proposed a unidirectional conducting canonical object to satisfy the requirements as a cross-polarized bistatic calibration device. Olk et al. [11] proposed a wire mesh with high cross-polarization level for the calibration of monostatic and bistatic radar cross section (RCS) facility operating at W-band. A mainlobe steered dihedral (MSD) object was proposed by Beaudoin et al. [12], which can be applied to bistatic polarimetric calibration. Kong and Xu [13] proposed a rhombus-shaped dihedral, which can be used for polarimetric calibration and background clutter extraction simultaneously. Ali and Perret [14] proposed an augmented depolarizing circular scatterer based on resonant elements, which performs well in a compact range. For improved calibration methods, Muth [15], [16] proposed a nonlinear calibration technique based on Fourier analysis, suppressing the effects of system drift and background clutter in measurement environment effectively. Wu and Xu [17] proposed an improved calibration technique for the case of quasi-monostatic polarimetric measurement system, which is very common in RCS test ranges.

For fully polarimetric calibration of a nonreciprocal radar system, there are eight distortion parameters needing to be solved, i.e., four crosstalk parameters and four polarization channel gain factors [9]. Measurements of a single traditional dihedral corner reflector cannot provide enough independent equations, resulting in requirement of a second nondepolarizing calibrator, such as a metal plate, sphere, or cylinder, and so on. In other words, the measurements of at least two different conventional calibrators are required for fully polarimetric calibration of a nonreciprocal radar system. Extra workload and complexity are added in polarimetric measurements when interchanging calibrators and concerning with the accurate position and orientation.

To simplify the measurement and calibration procedure, a new single polarimetric calibrator consisting of a quarter concave cylinder linked dihedral (QCCLD) reflector was first proposed by Wu and Xu [18], [19], which can accomplish

Manuscript received 31 July 2022; revised 3 December 2022; accepted 18 January 2023. Date of publication 31 January 2023; date of current version 7 April 2023. *(Corresponding author: Xiaojian Xu.)*

Xiaojian Xu and Tianjin Liu are with the School of Electronics and Information Engineering, Beihang University, Beijing 100191, China (e-mail: xiaojianxu@buaa.edu.cn; tianjinliu@buaa.edu.cn).

Pengfei Wu is with the Beijing Institute of Remote Sensing Equipment, Beijing 100039, China (e-mail: wupengfeibbi@sina.com).

Color versions of one or more figures in this article are available at https://doi.org/10.1109/TAP.2023.3240091.

Digital Object Identifier 10.1109/TAP.2023.3240091

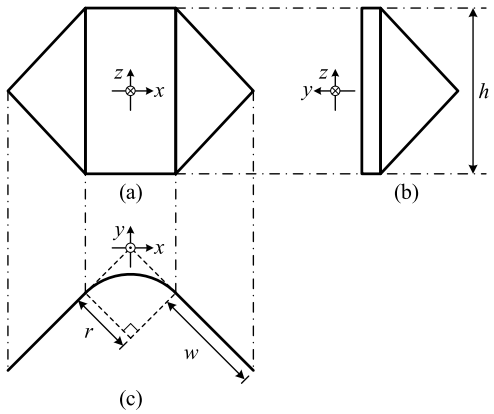

Fig. 1. Geometry of the QCCLD calibrator. (a) Frontal view. (b) Profile view. (c) Top view.

fully polarimetric calibration for nonreciprocal radar systems by measuring just itself. In this article, starting from our previous work, further in-depth studies of the QCCLD calibrator are made as follows. The scattering mechanisms are analyzed in detail. In addition, the theoretical PSM varying with rotation angle along the radar line of sight (LOS) is derived based on physical optics (PO). A novel polarimetric calibration procedure based on parametric representation using complex exponential (CE) model [20], [21], [22], [23] is presented to suppress the interference of undesirable scattering components for enhanced accuracy. Finally, experimental results are presented to validate the usefulness of the QCCLD polarimetric passive calibrator.

This article is organized as follows. The three-dimensional (3-D) geometry, theoretical PSM, and scattering mechanism of the proposed QCCLD calibrator are analyzed in Section II. In Section III, the polarimetric measurement signal model and the CE model parametric representation-based calibration procedure are presented. Experimental measurements and calibration results are illustrated in Section IV with analysis to validate the proposed QCCLD calibrator. We summarize this article in Section V.

II. Geometry, Theoretical PSM, and Scattering Mechanism of QCCLD

A. Geometry and Theoretical PSM

The previous work [19] has suggested that the frequency dispersion characteristic of a concave cylindrical surface is more stable than a metal plate. Besides, less diffraction wave and interaction with the concave cylinder are excited by a triangular-shaped dihedral than a rectangular-shaped one. As illustrated in Fig. 1, the QCCLD calibrator is designed as a combination of a separated triangular-shaped dihedral and a quarter of concave cylinder, which is determined by three parameters, i.e., the height h, the radius of the concave cylinder r, and the width of the triangular plate w.

When the calibrator is rotating with an angle of θ along the radar LOS, the PSM can be expressed as

$$\boldsymbol{S}(\theta) = S_{\text{cyl}}\begin{bmatrix} 1 & 0 \\ 0 & 1 \end{bmatrix} + S_{\text{dih}}\begin{bmatrix} -\cos 2\theta & \sin 2\theta \\ \sin 2\theta & \cos 2\theta \end{bmatrix} \tag{1}$$

TABLE I
Scattering Mechanisms of the QCCLD Calibrator

SC	Down range	Mechanism
1	$y_1 = -(\sqrt{2}-1)r$	Single-bounce reflection of the concave cylinder.
2	$y_2 = 0$	Double-bounce scattering of the separated dihedral.
3	$0 < y_3 < \frac{\sqrt{w^2+2r^2+2wr}}{2} - \frac{\sqrt{2}(w+2r)}{4}$	Double-bounce interaction between concave cylinder and dihedral.
4	$y_4 = (1-1/\sqrt{2})w + (\pi/4 - 1/\sqrt{2})r$	Travelling wave along the dihedral and concave cylinder.
5	$y_5 = -(\sqrt{2}-1)r$	Diffraction wave from the curved edge of the cylinder.
6	$y_6 = -r/\sqrt{2}$	Diffraction wave on the tip of plate-cylinder junction.
7	$y_7 = -(w+r)/\sqrt{2}$	Diffraction wave on the front tip of each triangular plate.
8	$y_8 = h/2 - (\sqrt{2}-1)r$	Travelling wave along the concave cylinder.

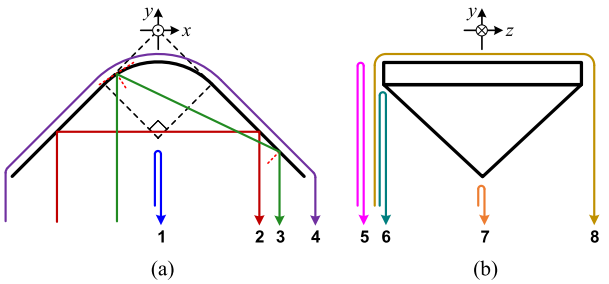

Fig. 2. Scattering mechanisms of the QCCLD. (a) Top view. (b) Profile view.

where S_{cyl} and S_{dih} are the scattering components of concave cylinder and dihedral at 0° rotation, respectively, which are derived in Appendix-A based on PO. Substitute (A13) and (A18) into (1), the theoretical backscattering PSM of the QCCLD calibrator can be written as

$$S_{\text{HH}}(\theta) = \text{j}\sqrt{\frac{r}{2\lambda}}he^{-\text{j}2k\left(1-\sqrt{2}\right)r} - \text{j}\frac{wh}{\sqrt{2}\lambda}\cos 2\theta \tag{2}$$

$$S_{\text{HV}}(\theta) = \text{j}\frac{wh}{\sqrt{2}\lambda}\sin 2\theta \tag{3}$$

$$S_{\text{VH}}(\theta) = \text{j}\frac{wh}{\sqrt{2}\lambda}\sin 2\theta \tag{4}$$

$$S_{\text{VV}}(\theta) = \text{j}\sqrt{\frac{r}{2\lambda}}he^{-\text{j}2k\left(1-\sqrt{2}\right)r} + \text{j}\frac{wh}{\sqrt{2}\lambda}\cos 2\theta \tag{5}$$

where H and V stand for horizontal and vertical polarizations, respectively.

B. Backscattering Mechanism Analysis

The backscattered field of QCCLD calibrator consists of four kinds of mechanisms, i.e., the specular reflection wave, the multiple reflection wave, the diffraction wave, and the surface wave. The scattering mechanisms are illustrated in Fig. 2, where the EM wave incidents along the y-axis. The number markers of different scattering centers (SCs) are detailed in Table I.

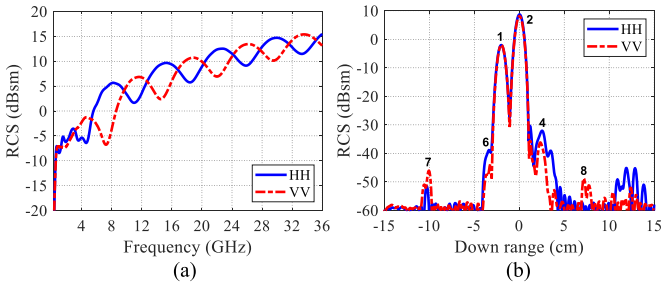

Fig. 3. Backscattering RCS and HRRP of QCCLD with 0° rotation. (a) RCS. (b) HRRP.

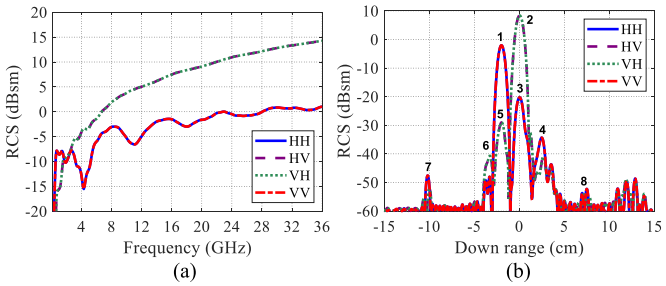

Fig. 4. Backscattering RCS and HRRP of QCCLD with 45° rotation. (a) RCS. (b) HRRP.

The ultrawideband (UWB) backscattering RCS from 100 MHz to 36 GHz with a 100 MHz frequency step of a specific QCCLD calibrator with $h = 190$ mm, $w = 96$ mm, and $r = 48$ mm is calculated using method of moment (MoM) code of FEKO software [24]. Fig. 3(a) and (b) shows the RCS and high-resolution range profile (HRRP) at 0° rotation. A Chebyshev window function is used to suppress the sidelobe. The RCS increasing with frequency shows a periodical oscillation characteristic due to the vector addition of SC1 and SC2, corresponding with (2) and (5) of the theoretical PSM. In addition, the traveling wave of SC8 can only be excited at VV polarization at this rotation angle [25]. Fig. 4(a) and (b) shows the RCS and HRRP at 45° rotation. It is seen that SC1 dominates in co-polarization component, while SC2 dominates in cross-polarization component. The fully polarimetric HRRP sequences of QCCLD calibrator varying with rotation angle along radar LOS are shown in Fig. 5, where Hamming window function is used. It is seen that the SC1 keeps constant, while the SC2 varies periodically with the rotation angle.

III. Polarimetric Measurement Signal Model and Calibration Procedure

A. Polarimetric Signal Model Based on QCCLD Calibrator

The measurement signal model for polarimetric calibration of a nonreciprocal radar system can be described in the form of matrices as [9]

$$\mathbf{M} = \mathbf{R}(\mathbf{S} + \mathbf{B})\mathbf{T} + \mathbf{N} \tag{6}$$

where $\mathbf{M}$ is the measurement signal matrix, $\mathbf{S}$ denotes the true PSM of target, and $\mathbf{T}$ and $\mathbf{R}$ represent the transmitting and receiving distortion matrices, respectively. The undesirable signals $\mathbf{B}$ and $\mathbf{N}$ stand for the clutter and noise matrices, respectively.

In practical measurements, the signal-to-noise ratio (SNR) can be high enough by pulse accumulation, so the effect of $\mathbf{N}$ can be ignored. The background clutter $\mathbf{B}$ of measurement environment can usually be well suppressed by vector subtraction or Fourier analysis method proposed by Muth [15], [16]. Then, the polarimetric measurement signal model can be simplified as

$$\mathbf{M} = \mathbf{RST} \tag{7}$$

with

$$\begin{bmatrix} M_{\mathrm{HH}} & M_{\mathrm{HV}} \\ M_{\mathrm{VH}} & M_{\mathrm{VV}} \end{bmatrix} = \begin{bmatrix} R_{\mathrm{HH}} & R_{\mathrm{HV}} \\ R_{\mathrm{VH}} & R_{\mathrm{VV}} \end{bmatrix} \begin{bmatrix} S_{\mathrm{HH}} & S_{\mathrm{HV}} \\ S_{\mathrm{VH}} & S_{\mathrm{VV}} \end{bmatrix} \times \begin{bmatrix} T_{\mathrm{HH}} & T_{\mathrm{HV}} \\ T_{\mathrm{VH}} & T_{\mathrm{VV}} \end{bmatrix}. \tag{8}$$

Normalize the receiving and transmitting distortion matrices as

$$\begin{bmatrix} R_{\mathrm{HH}} & R_{\mathrm{HV}} \\ R_{\mathrm{VH}} & R_{\mathrm{VV}} \end{bmatrix} = \begin{bmatrix} R_{\mathrm{HH}} & 0 \\ 0 & R_{\mathrm{VV}} \end{bmatrix} \begin{bmatrix} 1 & \varepsilon_{\mathrm{H}}^{\mathrm{R}} \\ \varepsilon_{\mathrm{V}}^{\mathrm{R}} & 1 \end{bmatrix} \tag{9}$$

$$\begin{bmatrix} T_{\mathrm{HH}} & T_{\mathrm{HV}} \\ T_{\mathrm{VH}} & T_{\mathrm{VV}} \end{bmatrix} = \begin{bmatrix} 1 & \varepsilon_{\mathrm{V}}^{\mathrm{T}} \\ \varepsilon_{\mathrm{H}}^{\mathrm{T}} & 1 \end{bmatrix} \begin{bmatrix} T_{\mathrm{HH}} & 0 \\ 0 & T_{\mathrm{VV}} \end{bmatrix} \tag{10}$$

where $\varepsilon_{\mathrm{H}}^{\mathrm{R}} = R_{\mathrm{HV}}/R_{\mathrm{HH}}$, $\varepsilon_{\mathrm{V}}^{\mathrm{R}} = R_{\mathrm{VH}}/R_{\mathrm{VV}}$, $\varepsilon_{\mathrm{H}}^{\mathrm{T}} = T_{\mathrm{VH}}/T_{\mathrm{HH}}$, and $\varepsilon_{\mathrm{V}}^{\mathrm{T}} = T_{\mathrm{HV}}/T_{\mathrm{VV}}$ refer to the crosstalk parameters of receiving and transmitting polarization channels.

The polarization channel gain matrix can be constructed by pointwise product as

$$\begin{bmatrix} g_{\mathrm{HH}} & g_{\mathrm{HV}} \\ g_{\mathrm{VH}} & g_{\mathrm{VV}} \end{bmatrix} = \begin{bmatrix} R_{\mathrm{HH}}T_{\mathrm{HH}} & R_{\mathrm{HH}}T_{\mathrm{VV}} \\ R_{\mathrm{VV}}T_{\mathrm{HH}} & R_{\mathrm{VV}}T_{\mathrm{VV}} \end{bmatrix} \tag{11}$$

where g_{HH}, g_{HV}, g_{VH}, and g_{VV} represent the polarization channel gain factors.

Therefore, the polarimetric calibration model with eight distortion parameters of a nonreciprocal radar system is expressed as

$$\begin{bmatrix} M_{\mathrm{HH}} & M_{\mathrm{HV}} \\ M_{\mathrm{VH}} & M_{\mathrm{VV}} \end{bmatrix} = \begin{bmatrix} g_{\mathrm{HH}} & g_{\mathrm{HV}} \\ g_{\mathrm{VH}} & g_{\mathrm{VV}} \end{bmatrix} \odot \begin{bmatrix} 1 & \varepsilon_{\mathrm{H}}^{\mathrm{R}} \\ \varepsilon_{\mathrm{V}}^{\mathrm{R}} & 1 \end{bmatrix} \begin{bmatrix} S_{\mathrm{HH}} & S_{\mathrm{HV}} \\ S_{\mathrm{VH}} & S_{\mathrm{VV}} \end{bmatrix} \times \begin{bmatrix} 1 & \varepsilon_{\mathrm{V}}^{\mathrm{T}} \\ \varepsilon_{\mathrm{H}}^{\mathrm{T}} & 1 \end{bmatrix} \tag{12}$$

where the operator $\odot$ stands for a Hadamard product.

Substitute the theoretical PSM of QCCLD into (12), we have

$$\begin{aligned} M_{\mathrm{HH}}(\theta) &= g_{\mathrm{HH}}\big[\big(\varepsilon_{\mathrm{H}}^{\mathrm{R}}\varepsilon_{\mathrm{H}}^{\mathrm{T}} - 1\big)S_{\mathrm{dih}}\cos 2\theta \\ &\quad + \big(\varepsilon_{\mathrm{H}}^{\mathrm{R}} + \varepsilon_{\mathrm{H}}^{\mathrm{T}}\big)S_{\mathrm{dih}}\sin 2\theta + \big(1 + \varepsilon_{\mathrm{H}}^{\mathrm{R}}\varepsilon_{\mathrm{H}}^{\mathrm{T}}\big)S_{\mathrm{cyl}}\big] \end{aligned} \tag{13}$$

$$\begin{aligned} M_{\mathrm{HV}}(\theta) &= g_{\mathrm{HV}}\big[\big(\varepsilon_{\mathrm{H}}^{\mathrm{R}} - \varepsilon_{\mathrm{V}}^{\mathrm{T}}\big)S_{\mathrm{dih}}\cos 2\theta \\ &\quad + \big(1 + \varepsilon_{\mathrm{H}}^{\mathrm{R}}\varepsilon_{\mathrm{V}}^{\mathrm{T}}\big)S_{\mathrm{dih}}\sin 2\theta + \big(\varepsilon_{\mathrm{H}}^{\mathrm{R}} + \varepsilon_{\mathrm{V}}^{\mathrm{T}}\big)S_{\mathrm{cyl}}\big] \end{aligned} \tag{14}$$

$$\begin{aligned} M_{\mathrm{VH}}(\theta) &= g_{\mathrm{VH}}\big[\big(\varepsilon_{\mathrm{H}}^{\mathrm{T}} - \varepsilon_{\mathrm{V}}^{\mathrm{R}}\big)S_{\mathrm{dih}}\cos 2\theta \\ &\quad + \big(1 + \varepsilon_{\mathrm{V}}^{\mathrm{R}}\varepsilon_{\mathrm{H}}^{\mathrm{T}}\big)S_{\mathrm{dih}}\sin 2\theta + \big(\varepsilon_{\mathrm{V}}^{\mathrm{R}} + \varepsilon_{\mathrm{H}}^{\mathrm{T}}\big)S_{\mathrm{cyl}}\big] \end{aligned} \tag{15}$$

$$\begin{aligned} M_{\mathrm{VV}}(\theta) &= g_{\mathrm{VV}}\big[\big(1 - \varepsilon_{\mathrm{V}}^{\mathrm{R}}\varepsilon_{\mathrm{V}}^{\mathrm{T}}\big)S_{\mathrm{dih}}\cos 2\theta \\ &\quad + \big(\varepsilon_{\mathrm{V}}^{\mathrm{R}} + \varepsilon_{\mathrm{V}}^{\mathrm{T}}\big)S_{\mathrm{dih}}\sin 2\theta + \big(1 + \varepsilon_{\mathrm{V}}^{\mathrm{R}}\varepsilon_{\mathrm{V}}^{\mathrm{T}}\big)S_{\mathrm{cyl}}\big]. \end{aligned} \tag{16}$$

B. Polarimetric Calibration Procedure

It is seen that the fully polarimetric measurement signals in (13) and (16) have the general form of

$$M_{\mathrm{pq}} = a_{\mathrm{pq}} + c_{\mathrm{pq}} \cos 2\theta + s_{\mathrm{pq}} \sin 2\theta \tag{17}$$

where the subscripts p and q stand for the electric polarization vectors either H or V for the receiver and transmitter.

The Fourier analysis method can be used to obtain all coefficients a_{pq}, c_{pq}, and s_{pq} from measurement data to suppress the effect of background clutter [15], [16]. The signal can be described as the Fourier series

$$M = a_0 + c_1 \cos\theta + s_1 \sin\theta + c_2 \cos 2\theta + s_2 \sin 2\theta + \cdots \tag{18}$$

Mathematically, the coefficients a_{pq}, c_{pq}, and s_{pq} of QCCLD calibrator correspond to a_0, c_2, and s_2 of each polarization [19]. Take HH polarization for example, we have

$$a_0^{\mathrm{HH}} = g_{\mathrm{HH}}\left(1 + \varepsilon_{\mathrm{H}}^{\mathrm{R}}\varepsilon_{\mathrm{H}}^{\mathrm{T}}\right) S_{\mathrm{cyl}} \tag{19}$$

$$c_2^{\mathrm{HH}} = g_{\mathrm{HH}}\left(\varepsilon_{\mathrm{H}}^{\mathrm{R}}\varepsilon_{\mathrm{H}}^{\mathrm{T}} - 1\right) S_{\mathrm{dih}} \tag{20}$$

$$s_2^{\mathrm{HH}} = g_{\mathrm{HH}}\left(\varepsilon_{\mathrm{H}}^{\mathrm{R}} + \varepsilon_{\mathrm{H}}^{\mathrm{T}}\right) S_{\mathrm{dih}}. \tag{21}$$

Assuming the calibrator rotates from 0 to 2π with $2N$ angle samples in measurement, the coefficients for any polarization can be calculated from measured data as

$$a_0^{\mathrm{pq}} = \frac{1}{2N} \sum_{\theta=0}^{2\pi} M_{\mathrm{pq}}(\theta) \tag{22}$$

$$c_2^{\mathrm{pq}} = \frac{1}{N} \sum_{\theta=0}^{2\pi} M_{\mathrm{pq}}(\theta) \cdot \cos 2\theta \tag{23}$$

$$s_2^{\mathrm{pq}} = \frac{1}{N} \sum_{\theta=0}^{2\pi} M_{\mathrm{pq}}(\theta) \cdot \sin 2\theta. \tag{24}$$

In fact, the coefficients a_0^{pq}, c_2^{pq}, and s_2^{pq} represent the three different scattering components of QCCLD for polarimetric calibration, i.e., a_0^{pq} is the constant component or the concave cylinder component, c_2^{pq} denotes the second-order cosinusoidal component or the dihedral component with 0° rotation, and s_2^{pq} denotes the second-order sinusoidal component or the dihedral component with 45° rotation.

The scattering components separated by Fourier analysis method from the rotated QCCLD MoM data shown in Fig. 5 are illustrated in Fig. 6. A Hamming window function is used to suppress the sidelobe in HRRPs.

It is seen from Fig. 6 that there are undesirable components excited by interaction, diffraction, and surface waves, resulting in RCS deviation deviating from the theoretical PSM derived from PO. For example, the interferential component in Fig. 6(b) at about 0 cm is caused by the double-bounce interaction between concave cylinder and dihedral, i.e., SC3 in Fig. 2. To suppress the interference of undesirable components, a CE model-based parametric representation approach [20], [21], [22], [23] is used to extract the main SC.

The CE model expression of target scattering function is

$$\sqrt{\sigma(f)} = \sum_{i=1}^{M} a_i e^{-\left(\alpha_i + \mathrm{j}\frac{4\pi r_i}{c}\right) f} \tag{25}$$

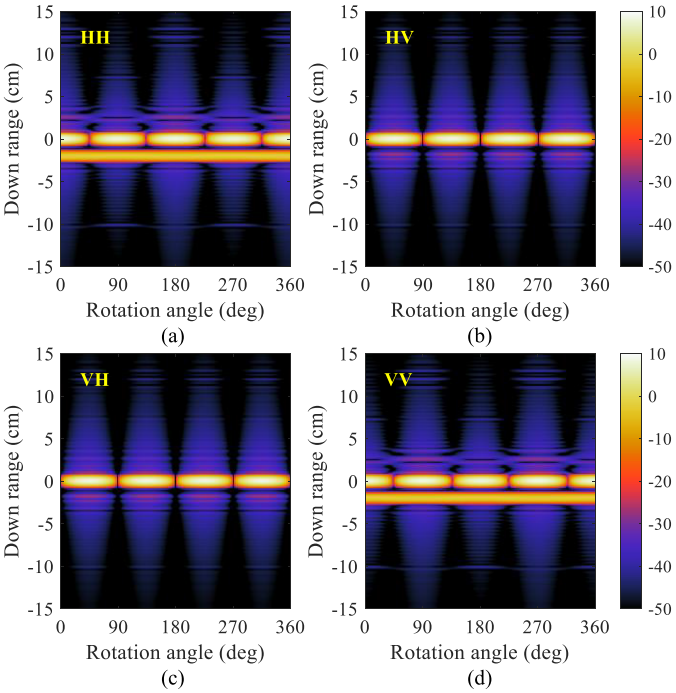

Fig. 5. Fully polarimetric HRRP sequences of QCCLD calibrator varying with rotation angle along radar LOS. (a) HH. (b) HV. (c) VH. (d) VV.

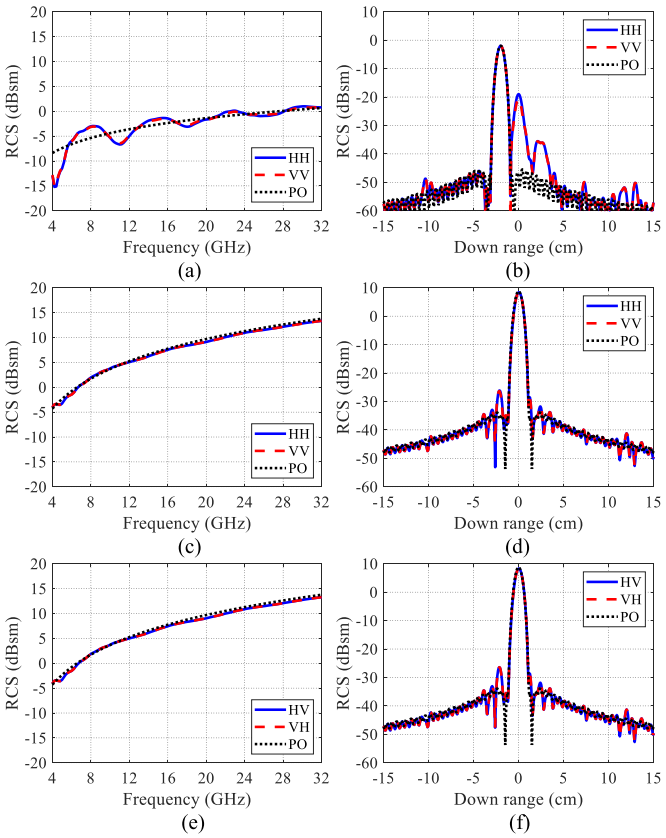

Fig. 6. Scattering components separation using the Fourier analysis method. (a) RCS and (b) HRRP of the constant component. (c) RCS and (d) HRRP of the second-order cosinusoidal component. (e) RCS and (f) HRRP of the second-order sinusoidal component.

where M is the model order or the number of scattering components;a_i, α_i, and r_i are the complex amplitude, the

frequency dispersion factor, and the distance from phase center of the ith SCs, respectively, which can be estimated by state space approach (SSA) [22]; f is the radar frequency vector.

Assuming that the kth SC can be reconstructed by the m_1th to m_2th scattering components, the scattering function of the kth SC can be written as

$$\sqrt{\sigma_k(f)} = \sum_{i=m_1}^{m_2} a_i e^{-\left(\alpha_i + \mathrm{j}\frac{4\pi r_i}{c}\right) f} \tag{26}$$

where m_1 and m_2 of the kth SC can be determined by the boundary locations r_{m1} and r_{m2} of the main lobe in the HRRP domain, respectively.

In practice, considering the widening of the main lobe caused by the distortion parameters (crosstalk parameters and channel gain factors), the locations r_{m1} and r_{m2} are obtained by the following mathematical optimization as:

$$\begin{aligned}
&[r_{m1},\ r_{m2}] \\
&\quad = \arg\min\{|\chi_1| + |\chi_2| + |\chi_3| + |\chi_4| + |\chi_5|\} \\
&\quad \text{subject to} \begin{cases}
\chi_1 = s_2^{\mathrm{HH}}/c_2^{\mathrm{HH}} - \left(\varepsilon_{\mathrm{H}}^{\mathrm{R}} + \varepsilon_{\mathrm{H}}^{\mathrm{T}}\right)/\left(\varepsilon_{\mathrm{H}}^{\mathrm{R}}\varepsilon_{\mathrm{H}}^{\mathrm{T}} - 1\right) \\
\chi_2 = c_2^{\mathrm{HV}}/s_2^{\mathrm{HV}} - \left(\varepsilon_{\mathrm{H}}^{\mathrm{R}} - \varepsilon_{\mathrm{V}}^{\mathrm{T}}\right)/\left(1 + \varepsilon_{\mathrm{H}}^{\mathrm{R}}\varepsilon_{\mathrm{V}}^{\mathrm{T}}\right) \\
\chi_3 = c_2^{\mathrm{VH}}/s_2^{\mathrm{VH}} - \left(\varepsilon_{\mathrm{H}}^{\mathrm{T}} - \varepsilon_{\mathrm{V}}^{\mathrm{R}}\right)/\left(1 + \varepsilon_{\mathrm{V}}^{\mathrm{R}}\varepsilon_{\mathrm{H}}^{\mathrm{T}}\right) \\
\chi_4 = s_2^{\mathrm{VV}}/c_2^{\mathrm{VV}} - \left(\varepsilon_{\mathrm{V}}^{\mathrm{R}} + \varepsilon_{\mathrm{V}}^{\mathrm{T}}\right)/\left(1 - \varepsilon_{\mathrm{V}}^{\mathrm{R}}\varepsilon_{\mathrm{V}}^{\mathrm{T}}\right) \\
\chi_5 = \left(a_0^{\mathrm{HV}}a_0^{\mathrm{VH}}\right)/\left(a_0^{\mathrm{HH}}a_0^{\mathrm{VV}}\right) \\
\qquad - \dfrac{\left(\varepsilon_{\mathrm{H}}^{\mathrm{R}} + \varepsilon_{\mathrm{V}}^{\mathrm{T}}\right)\left(\varepsilon_{\mathrm{V}}^{\mathrm{R}} + \varepsilon_{\mathrm{H}}^{\mathrm{T}}\right)}{\left(1 + \varepsilon_{\mathrm{H}}^{\mathrm{R}}\varepsilon_{\mathrm{H}}^{\mathrm{T}}\right)\left(1 + \varepsilon_{\mathrm{V}}^{\mathrm{R}}\varepsilon_{\mathrm{V}}^{\mathrm{T}}\right)} \\
r_{m2} + r_{m1} = 2r_{m0} \\
r_{m2} - r_{m1} > 0
\end{cases}
\end{aligned} \tag{27}$$

where r_{m0} is the peak value location of the main lobe in HRRP. The objective function is minimized by gradually increasing the distance between r_{m1} and r_{m2}.

The SC extraction result from Fig. 6 is shown in Fig. 7. It is seen that after SC extraction based on CE model parametric representation, the undesirable components are well suppressed and the main SCs agree well with the theoretical value of PO. In addition, the RCS uncertainty of CE model representation is shown in Appendix-B. After separation and extraction of the three scattering components for each polarization, the distortion parameters can be solved by the polarimetric calibration model described above.

The polarimetric calibration procedure for nonreciprocal radar systems using the QCCLD calibrator is summarized in four steps.

Step 1: Obtain the fully polarimetric measurement data from a nonreciprocal radar system of the QCCLD calibrator rotated along the radar LOS.

Step 2: Separate the scattering components using the Fourier analysis method. Then, extract the main SCs using CE model-based parametric representation approach.

Step 3: Solve the polarimetric calibration model to obtain the eight distortion parameters of the nonreciprocal radar system.

Step 4: Use the obtained distortion parameters for fully polarimetric calibration of the radar target under test.

The flowchart of the polarimetric calibration procedure is shown in Fig. 8.

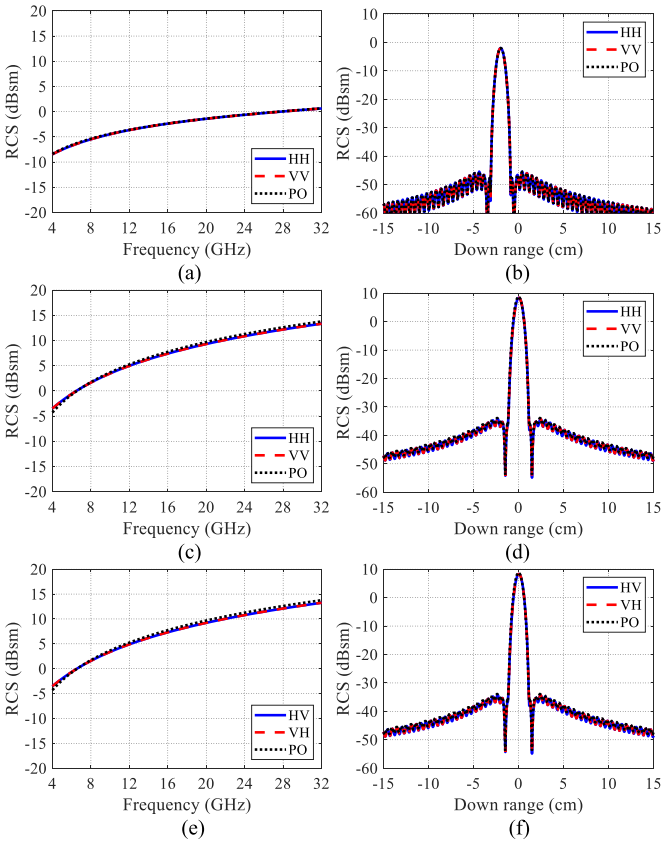

Fig. 7. SCs extraction using CE model-based parametric representation approach. (a) RCS and (b) HRRP of the constant component. (c) RCS and (d) HRRP of the second-order cosinusoidal component. (e) RCS and (f) HRRP of the second-order sinusoidal component.

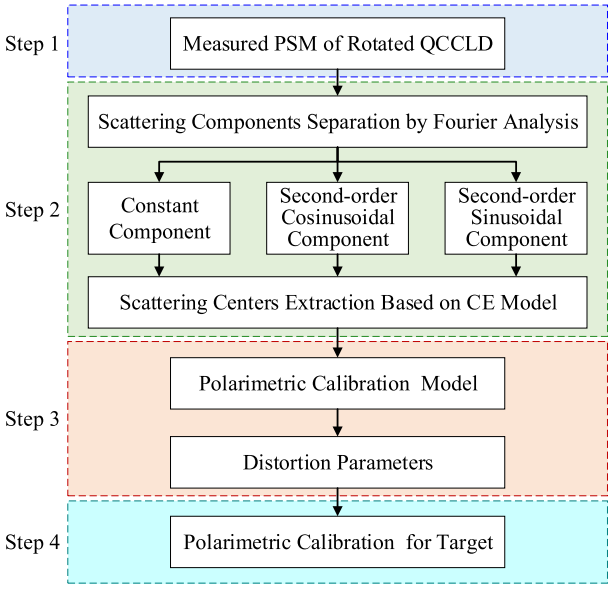

Fig. 8. Polarimetric calibration procedure.

IV. Experimental Results

The fully polarimetric measurement experiments based on the proposed QCCLD calibrator are carried out in an indoor test range. Fig. 9 illustrates the manufactured QCCLD calibrator and the nonreciprocal polarimetric radar system. The

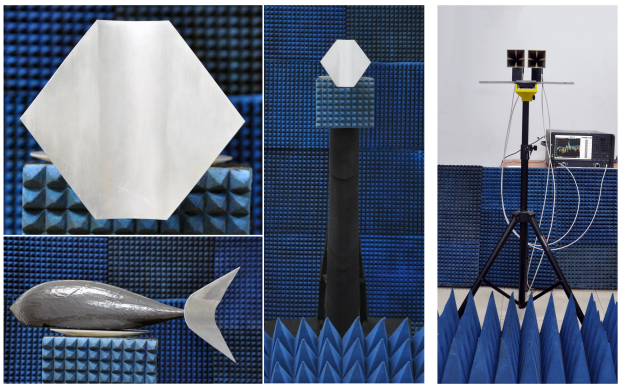

Fig. 9. Measurement on the manufactured QCCLD polarimetric calibrator. (a) QCCLD calibrator under test. (b) Polarimetric measurement system.

TABLE II
MEASUREMENT PARAMETERS

Parameters	Values
Measurement distance (m)	5.4
Radar frequency (GHz)	6.0 – 18.0
Frequency sampling points	1201
Rotation angle of QCCLD (deg)	0 – 360
Rotation angle sampling points	400

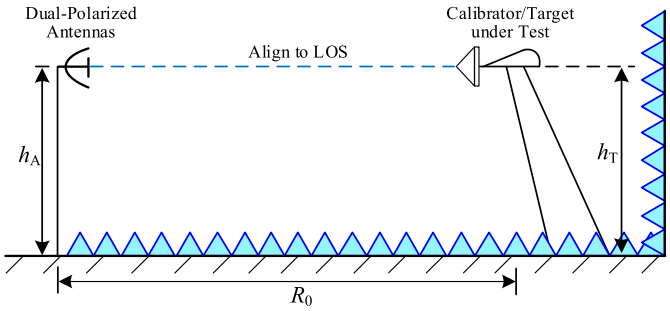

Fig. 10. Configuration of the measurement experiment.

size of the QCCLD is the same as described in Section II-B with $h = 190$ mm, $w = 96$ mm, and $r = 48$ mm. The radar system consists of two wideband dual-polarized horn antennas and a vector network analyzer (VNA). The size of the two antennas is 85 mm and the distance between them is 100 mm, resulting in a quasi-monostatic angle of 1.06°. The configuration of the experiment is illustrated in Fig. 10. The targets under calibration are a square metal plate sized 150 mm in width and a triangular-shaped dihedral whose height and width are 300 and 150 mm, respectively. The calibrator and targets under test are mounted on a metal pylon coated with radar absorbing material (RAM). The measurement parameters are listed in Table II.

Fig. 11 shows the measured fully polarimetric magnitude of the QCCLD calibrator at the center frequency of 12 GHz. It is seen that the mean values of the co-polarization signals are not zero due to the concave cylinder scattering component.

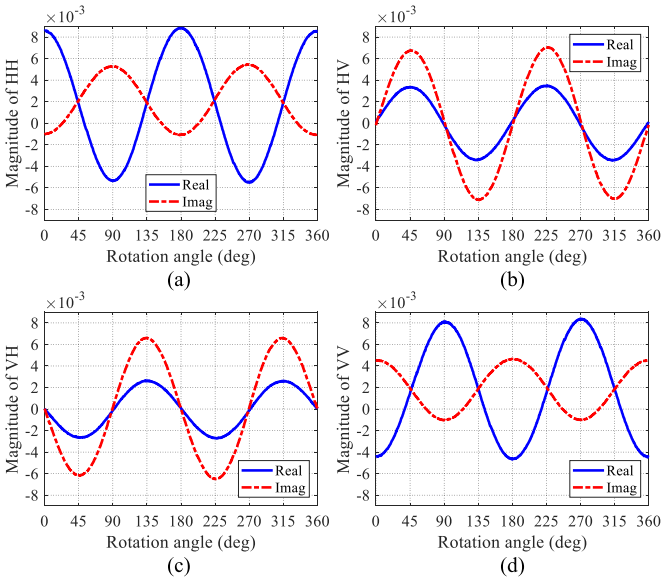

Fig. 11. Fully polarimetric measurement magnitudes of QCCLD varying with rotation angle at a center frequency of 12 GHz. (a) HH. (b) HV. (c) VH. (d) VV.

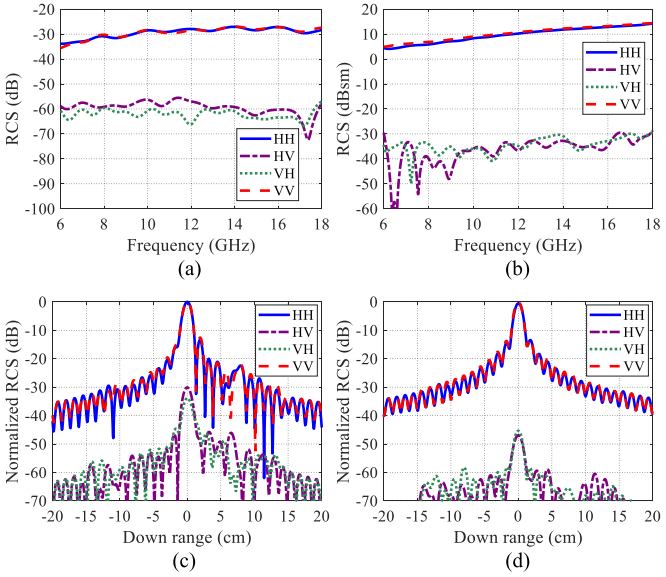

Fig. 12. Fully polarimetric calibration of a target square metal plate. (a) Before and (b) after polarimetric calibration of RCS curves. (c) Before and (d) after polarimetric calibration of normalized HRRPs.

Fig. 12 illustrates the measured and fully polarimetric calibrated data for a target square metal plate. It can be seen that, before calibration, the polarization isolation of the measured data is about 30 dB. On the other hand, after polarimetric calibration, it becomes more than 45 dB in most cases over the 6–18 GHz frequency band, 15 dB better than the raw data.

In Fig. 13, the results of a target triangular-shaped dihedral with 0° rotation before and after polarimetric calibration are presented, respectively. The dihedral is a dominant co-polarization target under this rotation. It is found that for most cases, the cross-polarization component is about 50 dB down from the co-polarization component after calibration, 20 dB better than the uncalibrated data.

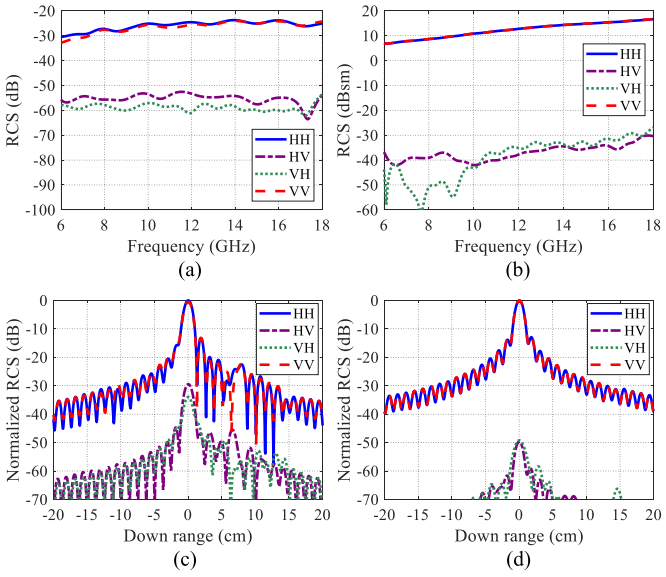

Fig. 13. Fully polarimetric calibration of a target triangular-shaped dihedral with 0° rotation. (a) Before and (b) after polarimetric calibration of RCS curves. (c) Before and (d) after polarimetric calibration of normalized HRRPs.

V. Conclusion

In this work, a new QCCLD calibrator is proposed for fully polarimetric calibration of nonreciprocal radar systems. The PSM of the calibrator consists of both depolarizing and nondepolarizing scattering components as rotating along the radar LOS. Therefore, fully polarimetric calibration for nonreciprocal radar systems can be accomplished through measurements of just a single QCCLD calibrator, greatly simplifying the measurement procedure. With the using of a CE model-based parametric representation, the interference of undesirable components is well suppressed during the fully polarimetric calibration process. Theoretical analysis and experimental results demonstrate that the QCCLD can be an excellent candidate for either indoor or outdoor uses.

Appendix

A. Theoretical PSM of QCCLD Based on PO Solution

The relationship between the target scattering matrix and RCS is shown as [26]

$$\sigma_{\mathrm{pq}} = 4\pi |S_{\mathrm{pq}}|^2 \tag{A1}$$

where S_{pq} denotes the element of the PSM, and σ_{pq} represents RCS.

According to the PO theory [25], the element of the PSM can be expressed as

$$S = \mathrm{j}\frac{k}{2\pi}\iint_A \hat{n}_s \cdot \hat{e}_r \times \hat{h}_i \cdot e^{-\mathrm{j}k\vec{r}(\hat{i}-\hat{s})} da \tag{A2}$$

where

k wavenumber;
$\hat{n}_s$ unit normal of the illuminated surface;
$\hat{e}_r$ unit vector along scattering polarization;
$\hat{h}_i$ unit vector of incident magnetic field;
$\vec{r}$ position vector from origin to the surface patch da;
$\hat{i}$ unit vector of incident wave;

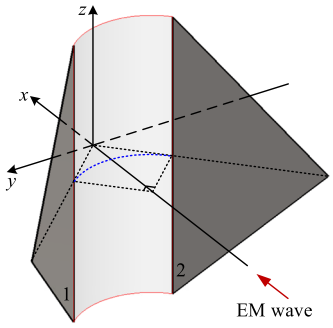

Fig. 14. Separated dihedral component of the QCCLD calibrator.

$\hat{s}$ unit vector of scattering wave;
A illuminated region of the surface.

For the separated dihedral component, considering the location of double-bounce scattering as the phase reference center, the Cartesian coordinate system xyz is established in Fig. 14.

Suppose that the incident EM wave first illuminates the left plate, then reflect to the right plate and finally back to the receiver, the scattering component can be expressed as

$$S_{12} = \mathrm{j}\frac{k}{2\pi}\hat{n}_2 \cdot \hat{e}_r \times \hat{h}_i \int_r^{r+w}\int_{-h\frac{r+w-m}{2w}}^{+h\frac{r+w-m}{2w}} \times e^{-\mathrm{j}k\vec{r}_2\cdot[\hat{i}-2(\hat{i}\cdot\hat{n}_1)\hat{n}_1-\hat{s}]} dndm \tag{A3}$$

where dm and dn are the integral elements along the direction of width and height, respectively.

In Fig. 14, the unit normals of the separated left and right triangular-shaped plates are, respectively

$$\hat{n}_1 = \left(-\sin\frac{\pi}{4}, -\cos\frac{\pi}{4}, 0\right) \tag{A4}$$

$$\hat{n}_2 = \left(-\sin\frac{\pi}{4}, \cos\frac{\pi}{4}, 0\right). \tag{A5}$$

The position vectors of the two plates can be written as

$$\vec{r}_1 = \left(-m\cos\frac{\pi}{4}, m\sin\frac{\pi}{4}, n\right) \tag{A6}$$

$$\vec{r}_2 = \left(-m\cos\frac{\pi}{4}, -m\sin\frac{\pi}{4}, n\right). \tag{A7}$$

In the case of backscattering, the unit vectors of incident and scattering waves are

$$\hat{i} = (1, 0, 0) \tag{A8}$$

$$\hat{s} = (-1, 0, 0). \tag{A9}$$

For H or V polarization, the vector product in (A3) can be written as

$$|\hat{e}_r \times \hat{h}_i| = (1, 0, 0). \tag{A10}$$

Substitute (A4)–(A10) into (A3), the double integral is derived as

$$\int_r^{r+w}\int_{-h\frac{r+w-m}{2w}}^{+h\frac{r+w-m}{2w}} e^{-\mathrm{j}k\vec{r}_2\cdot[\hat{i}-2(\hat{i}\cdot\hat{n}_1)\hat{n}_1-\hat{s}]} dndm = \frac{wh}{2}. \tag{A11}$$

Substitute (A11) into (A3), we get

$$S_{12} = \mathrm{j}\frac{wh}{2\sqrt{2}\lambda}. \tag{A12}$$

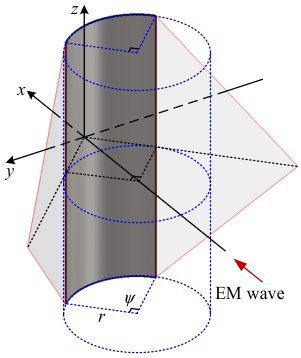

Fig. 15. Quarter concave cylinder component of the QCCLD calibrator.

Considering the scattering component that the incident EM wave first illuminates the right plate, we have $S_{21} = S_{12}$. Therefore, the separated dihedral component of QCCLD can be derived as

$$S_{\text{dih}} = \text{j}\frac{wh}{\sqrt{2}\lambda}. \tag{A13}$$

The concave cylinder component is a quarter of cylindrical surface from a right circular cylinder, whose height and radius are h and r, respectively, shown in Fig. 15.

The PO integral of the quarter concave cylinder component can be expressed as

$$S_{\text{cyl}} = \text{j}\frac{krh}{2\pi} e^{-\text{j}k\vec{r}_0(\hat{i}-\hat{s})} \int_{\psi} \hat{n}\cdot\hat{e}_r \times \hat{h}_i e^{-\text{j}kr\hat{n}(\hat{i}-\hat{s})} d\varphi. \tag{A14}$$

In the case of backscattering, considering the angle limit of the integral, (A14) can be simplified as

$$S_{\text{cyl}} = \text{j}\frac{krh}{2\pi} e^{\text{j}2k\sqrt{2}\,r} \int_{-\psi/2}^{+\psi/2} e^{-\text{j}2kr\cos\varphi} d\varphi. \tag{A15}$$

Stationary phase method is used to solve the integral in (A15). The phase function can be expanded in a Taylor series, and all terms beyond the second derivative are ignored. The stationary phase method can be described as [25]

$$\int g(\phi) e^{-\text{j}f(\phi)} d\phi \simeq \left[\frac{2\pi}{\text{j}f''(\phi_0)}\right]^{1/2} g(\phi_0) e^{-\text{j}f(\phi_0)}. \tag{A16}$$

The integral in (A15) can be solved as

$$\int_{-\psi/2}^{+\psi/2} e^{-\text{j}2kr\cos\varphi} d\varphi = \left[\frac{\lambda}{2r}\right]^{1/2} e^{-\text{j}2kr}. \tag{A17}$$

Substitute (A17) into (A15), the concave cylinder component of QCCLD can be written as

$$S_{\text{cyl}} = \text{j}\sqrt{\frac{r}{2\lambda}} \cdot h e^{-\text{j}2k\left(1-\sqrt{2}\right)r}. \tag{A18}$$

When the QCCLD is rotating along the radar LOS, the PSM can be expressed as (2)–(5) in Section II-A.

B. RCS Uncertainty of CE Model Parametric Representation

In Section III-B, the CE model-based parametric representation approach is used to extract SCs of the three scattering components of QCCLD calibrator for each polarization. Here, the RCS error caused by CE model is defined as

$$\varepsilon_{\text{CE}}(f) = \frac{\sigma_{\text{CE}}(f)}{\sigma_{\text{MoM}}(f)}. \tag{A19}$$

Take HH polarization as an example for the constant and the second-order cosinusoidal components and HV polarization as an example for the second-order sinusoidal component, the RCS error caused by CE model parametric representation is illustrated in Fig. 16. It is seen that the RCS uncertainty is within ±0.01 dB, which is accurate enough for polarimetric calibration.

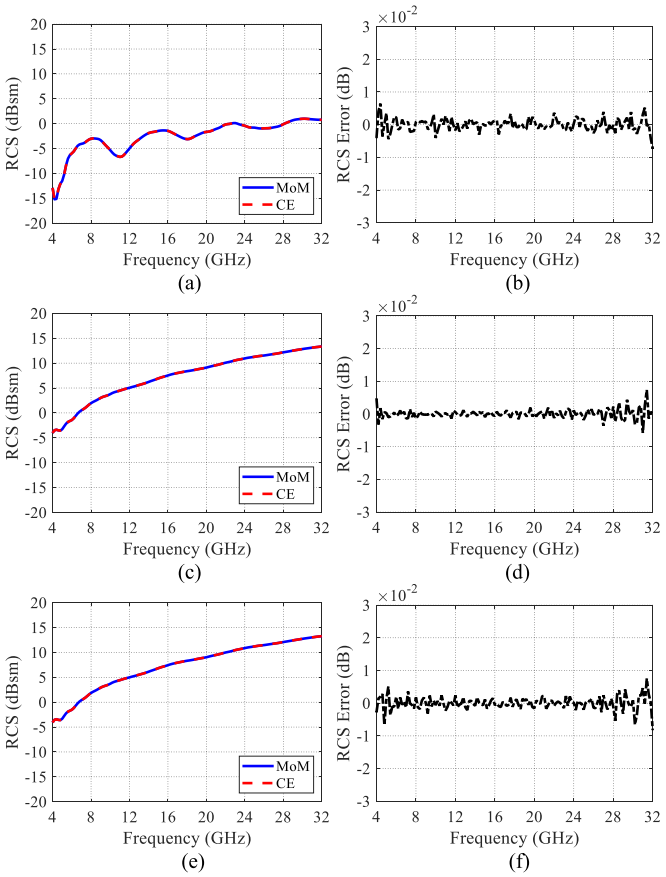

Fig. 16. RCS error caused by CE model parametric representation approach. (a) RCS and (b) error of the constant component. (c) RCS and (d) error of the second-order cosinusoidal component. (e) RCS and (f) error of the second-order sinusoidal component.

C. Calibration Sensitivity Analysis of a Rotating QCCLD

In practical applications of the rotating QCCLD, the calibration accuracy is related to various factors, including the location and posture of the calibrator, and the bistatic angle between the transmitting and receiving antennas, and so on. For instance, the incident EM wave can deviate from the expected orientation due to the imprecise placement of the calibrator. In this section, the calibration sensitivity of the rotating QCCLD is analyzed considering the RCS error and polarization purity affected by the monostatic, bistatic, and rotation angular errors.

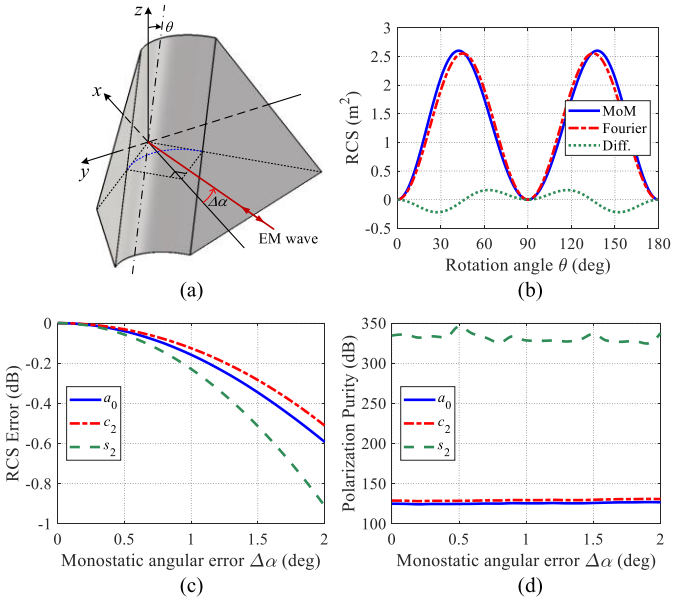

Fig. 17. Monostatic angular sensitivity of QCCLD. (a) Geometry of monostatic angular error. (b) RCS versus rotation angle of HV polarization with $\Delta\alpha = 2^{o}$. (c) RCS error and (d) polarization purity varying with monostatic angular error.

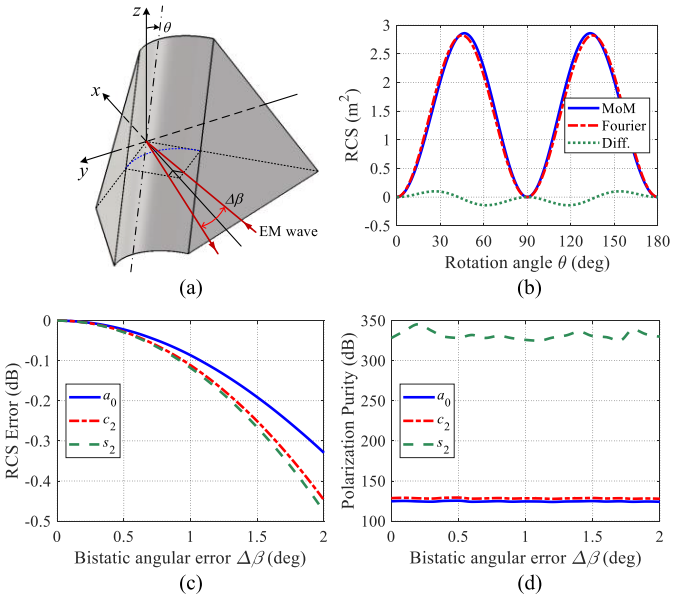

Fig. 18. Bistatic angular sensitivity of QCCLD. (a) Geometry of bistatic angular error. (b) RCS versus rotation angle of HV polarization with $\Delta\beta = 2^{o}$. (c) RCS error and (d) polarization purity varying with bistatic angular error.

1) Monostatic Angular Sensitivity: The radar EM wave with a monostatic angular error of $\Delta\alpha$ is illustrated in Fig. 17(a), where the QCCLD is rotating along the expected LOS with an angle of θ. The RCS characteristics are calculated using the MoM code of FEKO software [24] at the central frequency of 12 GHz of our experiment for HH and HV polarizations. The HV polarization RCS versus rotation angle with $\Delta\alpha = 2^{o}$ is shown in Fig. 17(b), demonstrating the RCS curves of the MoM result, the Fourier analysis result, and the difference between them. Using Fourier analysis method, the RCS error and the polarization purity versus monostatic angular error of constant, second-order cosinusoidal, and second-order sinusoidal components are illustrated, respectively, in Fig. 17(c) and (d).

It is seen from Fig. 17 that, with the angular error, an extra fourth-order sinusoidal component occurs [17]. Besides, the monostatic angular error of up to 0.7° is allowed for the RCS errors of all the three components less than 0.1 dB. In our experiment, the accessible accuracy can be better than ±0.1° using an electronic total station, so this error can be neglected. In addition, as seen from Fig. 17(d), the monostatic angular error of up to 2° makes no influence on the polarization purity.

2) Bistatic Angular Sensitivity: A symmetrical bistatic angle of $\Delta\beta$ between incident and scattering EM waves is illustrated in Fig. 18(a). The bistatic angle-sensitive RCS characteristics of QCCLD are shown in Fig. 18(b)–(d).

From Fig. 18, the bistatic angular error of less than 1° is allowed for the RCS error no more than about 0.1 dB. In the experiment, a bistatic angle of 1.06° is formed because of the separation between transmitter and receiver. In practice, either increasing measurement distance or closer installation of the two antennas can reduce the impact of bistatic angular error. In addition, it seems that a bistatic angular error of up to 2° makes no noticeable influence on the polarization purity.

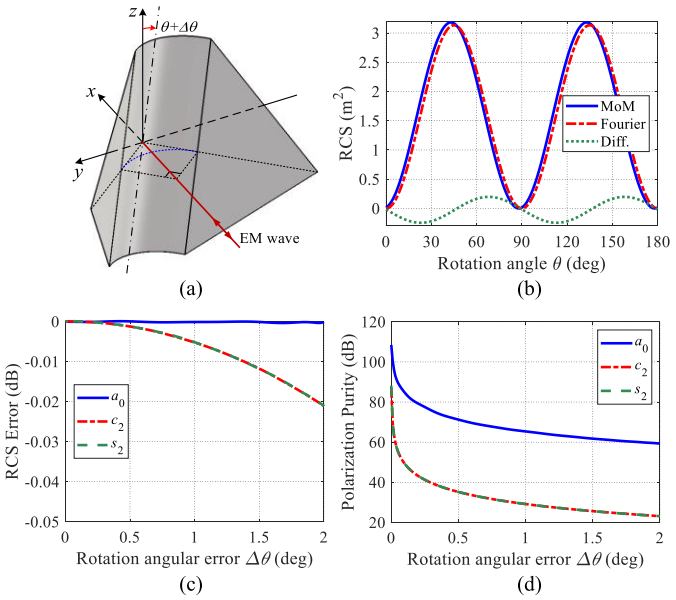

Fig. 19. Rotation angular sensitivity of QCCLD. (a) Geometry of rotation angular error. (b) RCS versus rotation angle of HV polarization with $\Delta\theta = 2^{o}$. (c) RCS error and (d) polarization purity varying with rotation angular error.

3) Rotation Angular Sensitivity: A misaligned rotation angle error of $\Delta\theta$ on the rotating QCCLD is shown in Fig. 19(a). The RCS characteristics in this case are shown in Fig. 19(b)–(d).

In Fig. 19(c), it is seen that the RCS error caused by the rotation angular error of up to 2° impacts little on the calibration by using the Fourier analysis method. However, this angular error makes a severe impact on the polarization purity, as seen from Fig. 19(d), where it is found that a rotation

angular error of less than 0.1° is allowable for a polarization purity better than 50 dB. The accessible mechanical accuracy of rotation angle can be about ±0.1° by using a digital gradienter in our experiment.

In general, the quality of polarimetric calibration depends on the exact position, orientation, and alignment of the rotating QCCLD. In practical applications, the calibration error can be effectively reduced by a careful installation with high-precision instruments and using the Fourier analysis method.

REFERENCES

[1] J.-S. Lee, E. Krogager, T. L. Ainsworth, and W. M. Boerner, "Polarimetric analysis of radar signature of a manmade structure," *IEEE Geosci. Remote Sens. Lett.*, vol. 3, no. 4, pp. 555–559, Oct. 2006.

[2] X. Y. Wang, T. Dallmann, R. Moch, and D. Heberling, "ISAR tomography for full-polarimetric 3-D radar cross-section measurements," *IEEE Trans. Antennas Propag.*, vol. 67, no. 4, pp. 2853–2858, Apr. 2019.

[3] W. Wiesbeck and S. Riegger, "A complete error model for free space polarimetric measurements," *IEEE Trans. Antennas Propag.*, vol. 39, no. 8, pp. 1105–1111, Aug. 1991.

[4] W. Wiesbeck and D. Kahny, "Single reference, three target calibration and error correction for monostatic, polarimetric free space measurements," *Proc. IEEE*, vol. 79, no. 10, pp. 1551–1558, Oct. 1991.

[5] T.-J. Chen, T.-H. Chu, and F.-C. Chen, "A new calibration algorithm of wide-band polarimetric measurement system," *IEEE Trans. Antennas Propag.*, vol. 39, no. 8, pp. 1188–1192, Aug. 1991.

[6] C. M. H. Unal, R. J. Niemeijer, J. S. van Sinttruyen, and L. P. Ligthart, "Calibration of a polarimetric radar using a rotatable dihedral corner reflector," *IEEE Trans. Geosci. Remote Sens.*, vol. 32, no. 4, pp. 837–845, Jul. 1994.

[7] J.-R. J. Gau and W. D. Burnside, "New polarimetric calibration technique using a single calibration dihedral," *IEE Proc. Microw., Antennas Propag.*, vol. 142, no. 1, pp. 19–25, Feb. 1995.

[8] B. M. Welsh, B. M. Kent, and A. L. Buterbaugh, "Full polarimetric calibration for radar cross-section measurements: Performance analysis," *IEEE Trans. Antennas Propag.*, vol. 52, no. 9, pp. 2357–2365, Sep. 2004.

[9] X. Xu, "Polarization measurement and calibration technique," in *New Techniques for Radar Target Scattering Signature Measurement and Processing*. Beijing, China: National Defense Industry Press, 2017, pp. 326–374.

[10] C. Monzon, "A cross-polarized bistatic calibration device for RCS measurements," *IEEE Trans. Antennas Propag.*, vol. 51, no. 4, pp. 833–839, Apr. 2003.

[11] A. Olk, K. B. Khadhra, and T. Spielmann, "Highly accurate fully-polarimetric radar cross section facility for mono- and bistatic measurements at W-band frequencies," in *Proc. Antenna Meas. Tech. Assoc. Symp. (AMTA)*, Atlanta, GA, USA, Oct. 2017, pp. 1–6.

[12] C. Beaudoin, T. Horgan, G. Demartinis, M. J. Coulombe, A. J. Gatesman, and W. E. Nixon, "Fully polarimetric bistatic radar calibration with modified dihedral objects," *IEEE Trans. Antennas Propag.*, vol. 66, no. 2, pp. 937–950, Feb. 2018.

[13] L. Kong and X. Xu, "A new dihedral reflector for simultaneous polarimetric calibration and background clutter extraction," in *Proc. IEEE Int. Symp. Antennas Propag. USNC/URSI Nat. Radio Sci. Meeting*, Jul. 2018, pp. 2461–2462.

[14] Z. Ali and E. Perret, "Augmented depolarizing scatterer based on resonant elements for polarimetric radar calibration," *IEEE Trans. Antennas Propag.*, vol. 70, no. 2, pp. 1415–1427, Feb. 2022.

[15] L. A. Muth, "Polarimetric calibration of indoor and outdoor polarimetric radar cross section systems," in *Proc. Antenna Meas. Techn. Assoc. (AMTA)*, Boston, MA, USA, Nov. 2008, pp. 37–42.

[16] L. A. Muth, "Nonlinear calibration of polarimetric radar cross section measurement systems," *IEEE Antennas Propag. Mag.*, vol. 52, no. 3, pp. 187–192, Jun. 2010.

[17] P. Wu and X. Xu, "Improved calibration technique for quasi-monostatic polarimetric measurement system using a dihedral as the calibration reference," *IEEE Trans. Antennas Propag.*, vol. 67, no. 11, pp. 7040–7049, Nov. 2019.

[18] P. Wu and X. Xu, "A new polarimetric passive radar calibrator for fully polarimetric measurement," in *Proc. SPIE*, Berlin, Germany, vol. 10800, Oct. 2018, pp. 39–48.

[19] P. Wu, "Research of RCS calibration and polarimetric calibration technique for static test range," Ph.D. dissertation, Dept. Elect. Electron. Eng., Beihang Univ., Beijing, China, 2019.

[20] K. Naishadham and J. E. Piou, "A robust state space model for the characterization of extended returns in radar target signatures," *IEEE Trans. Antennas Propag.*, vol. 56, no. 6, pp. 1742–1751, Jun. 2008.

[21] K. Naishadham and J. E. Piou, "Analytical characterization and validation of creeping waves on dielectric coated and perfectly conducting cylinders," *Radio Sci.*, vol. 45, no. 5, pp. 1–19, Oct. 2010.

[22] X. Xu, Z. Xie, and F. He, "Fast and accurate RCS calculation for squat cylinder calibrators [measurements corner]," *IEEE Antennas Propag. Mag.*, vol. 57, no. 1, pp. 33–41, Feb. 2015.

[23] T. Liu, X. He, and X. Xu, "Comprehensive characterization of an ellipsoidal cylinder calibrator for radar cross section measurement," *IEEE Trans. Antennas Propag.*, vol. 70, no. 9, pp. 8400–8414, Sep. 2022.

[24] FEKO, Stellenbosch, South Africa. (2014). EM Software & Systems-S.A. Accessed: Feb. 27, 2015. [Online]. Available: http://www.feko.info

[25] E. F. Knott, J. F. Shaeffer, and M. T. Tuley, "High-frequency RCS prediction techniques," in *Radar Cross Section*. 2nd ed. Raleigh, NC, USA: Scitech, 2004, pp. 183–224.

[26] G. T. Ruck, D. E. Barrick, W. D. Stuart, and C. K. Krichbaum, "Theory," in *Radar Cross Section Handbook*, vol. 1. New York, NY, USA: Plenum Press, 1970, pp. 7–139.

Xiaojian Xu was born in Jiangxi, China, in 1963. He received the B.S. degree from the Hefei University of Technology, Hefei, China, in 1983, the M.S. degree from the Beijing Institute of Environmental Features (BIEF), Beijing, China, in 1986, and the Ph.D. degree from the University of Nebraska-Lincoln, Lincoln, NE, USA, in 2002, all in electrical engineering.

From 1986 to 1999, he was with BIEF, where he was mainly involved in research of electromagnetic scattering modeling and microwave imaging. From June 1999 to December 2002, he was with the Environmental Remote Sensing Laboratory, University of Nebraska-Lincoln, where his research work was on ultrawideband random noise radar with emphasis on foliage and ground penetration applications. Since January 2003, he has been with the School of Electronic and Information Engineering, Beihang University, Beijing, as a Signal and Information Processing Professor. His research interests include remote sensing signatures, radar imagery, target recognition, and system modeling.

Tianjin Liu was born in Shandong, China, in 1996. He received the B.S. degree from the School of Information Science and Technology, Dalian Maritime University, Liaoning, China, in 2019. He is currently pursuing the Ph.D. degree in signal and information processing with the School of Electronics and Information Engineering, Beihang University, Beijing, China.

His research interests include RCS measurement, polarimetric calibration, and radar imaging.

Pengfei Wu was born in Beijing, China, in 1988. He received the B.S. degree in electronic information and control engineering from the Beijing University of Technology, Beijing, in 2010, and the Ph.D. degree in signal and information processing from the School of Electronics and Information Engineering, Beihang University, Beijing, in 2019.

His research interests include RCS measurement and polarimetric calibration.